Tectonophysics xxx (2009) xxx–xxx

Contents lists available at ScienceDirect

Tectonophysics

journal homepage: www.elsevier.com/locate/tecto

Body-wave tomography of western Canada

J.-P. Mercier [a], M.G. Bostock [a,*], J.F. Cassidy [b], K. Dueker [c], J.B. Gaherty [d], E.J. Garnero [e], J. Revenaugh [f], G. Zandt [g]

[a] Department of Earth and Ocean Sciences, The University of British Columbia, 6339 Stores Road, Vancouver, BC, Canada, V6T 1Z4
[b] Pacific Geoscience Center, 9860 West Saanich Road, P.O. Box 6000, Room 4707 Sidney, BC, Canada V8L 4B2
[c] Geology and Geophysics Department, University of Wyoming, Department 3006, 1000 East University Avenue, Laramie, WY 82071, United States
[d] Lamont-Doherty Earth Observatory, 61 Route 9, West Palisades, NY 10964, United States
[e] School of Earth and Space Exploration, Arizona State University, Tempe, AZ 85287, United States
[f] Department of Geology and Geophysics, University of Minnesota, 310 Pillsbury Drive SE, Minneapolis, MN 55455-0219, United States
[g] Department of Geosciences, University of Arizona, Tucson, AZ 85725, United States

ARTICLE INFO

Article history:
Received 17 October 2008
Received in revised form 27 March 2009
Accepted 8 May 2009
Available online xxxx

Keywords:
Body-wave tomography
Western Canada
Cordillera/craton transition
Cascadia subduction zone
Anahim volcanic belt

ABSTRACT

In this study, we have produced *P*- and *S*-wave velocity models for western Canada using 23,420 delay times measured on vertical component seismograms, and 15,805 delay times measured on transverse component seismograms, respectively, from a range of permanent and temporary networks. Resolution is best in southwestern British Columbia, and along the CANOE (northwestern Alberta, southern Yukon and Northwest Territories) and BATHOLITHS (northwestern BC) arrays where the station density is the highest, and fair elsewhere. We focus our attention on two distinct features 1) the transition from Phanerozoic to Cratonic mantle in northwestern Canada, and 2) the complex tectonic environment at the northern terminus of the Cascadia subduction zone where the plate boundary changes from convergent to transform. We find that the main transition from Phanerozoic to Cratonic mantle in northwestern Canada occurs at the Cordilleran deformation front and represents a sharp jump in seismic velocity from −2% to +2% over a distance of ~50 km. In northern Cascadia, we have imaged and characterized the signature of the subducting Juan de Fuca plate and observed evidence of subduction beyond the northern edge of the slab. We also demonstrate that the Anahim hotspot track is underlain by a −2% low-velocity zone possibly extending to 400 km beneath Nazko cone that appears to be the source of volcanism in this area. Consequently, we associate the source of magmatism in this area to a mantle-scale rather than lithospheric-scale process.

1. Introduction

Continents, unlike ocean basins, possess a protracted and complex tectonic evolution that is encoded within seismic velocity heterogeneity of the crust and underlying mantle. Western Canada is particularly rich in its structural make-up and represents the most nearly continuous sampling of Earth's geologic history over the past 4.0 Ga (see Fig. 1). Accordingly, the region affords an ideal setting to study subsurface variations in upper-mantle structure, geometry and physical properties from Archean to the present day. Moreover, the western margin also provides an opportunity to explore the complex transition from convergent to transform plate boundary. In this paper we employ regional body-wave tomography to investigate mantle velocity structure beneath western Canada.

Studies of western Canada upper-mantle velocity structure began more than 3 decades ago when Buchbinder and Poupinet (1977), Wickens (1977), and Wickens and Buchbinder (1980) used short-period *P*-waves, surface-wave, and long-period *S*-wave traveltime residuals, respectively, to document a low-velocity region beneath British Columbia. More recently, global and continental-scale studies that include western Canada, using both body-waves (e.g. Grand, 1994; Grand et al., 1997), and surface-waves (e.g. Frederiksen et al., 2001; van der lee and Frederiksen, 2005) have imaged a relatively sharp mantle transition from low to high velocity across the Cordilleran deformation front. At finer scales Bostock and VanDecar (1995) utilized body-wave traveltimes to constrain the geometry of the subducting Juan de Fuca plate below southwestern British Columbia whereas Frederiksen et al. (1998) and Shragge et al., (2002) focused on details of upper mantle velocity structure beneath the southern Yukon and south-central Alberta, respectively.

These previous studies have provided useful insights into western Canadian lithospheric and upper-mantle structure but are either global/continental-scale and suffer from low resolution, or local and lack a broader perspective. Until recently, the station density in most of western Canada precluded the undertaking of a comprehensive

* Corresponding author.
E-mail addresses: jmercier@eos.ubc.ca (J.-P. Mercier), mbostock@eos.ubc.ca (M.G. Bostock), jcassidy@nrcan-rncan.gc.ca (J.F. Cassidy), dueker@uwyo.edu (K. Dueker), gaherty@ldeo.columbia.edu (J.B. Gaherty), garnero@asu.edu (E.J. Garnero), justinr@umn.edu (J. Revenaugh), gzandt@email.arizona.edu (G. Zandt).

0040-1951/$ – see front matter © 2009 Elsevier B.V. All rights reserved.
doi:10.1016/j.tecto.2009.05.030

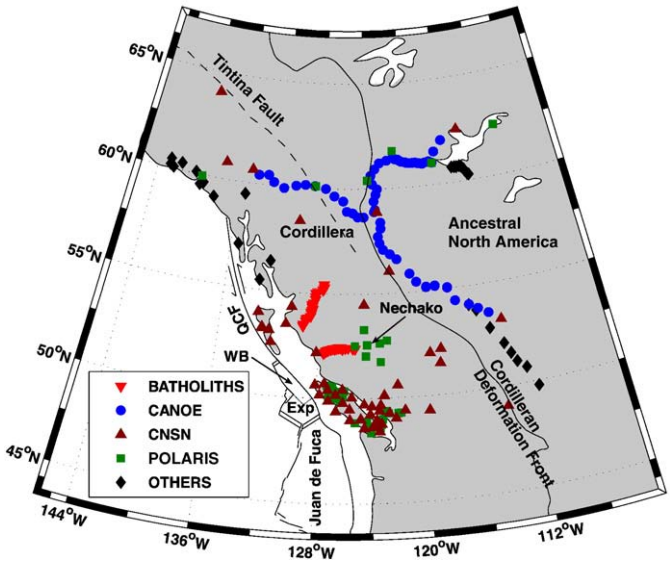

Fig. 1. Map of western Canada illustrating the distribution of broadband and short-period seismic stations used in this study, and the location of key tectonic features discussed in the text.(Exp: Explorer Plate, QCF: Queen Charlotte Fault, WB: Winona Block).

body-wave study over the entire region as performed for example, in the western United States (Humphreys and Dueker, 1994). However, the recent deployment of stations from several portable experiments (i.e. CANOE, BATHOLITHS, POLARIS BC and POLARIS-Nechako) have contributed to filling some major gaps in station coverage and afford opportunity for a broader scale study. In this paper, we exploit both newly available and previously analysed broadband and short-period data to examine the large-scale, upper-mantle *P*- and *S*-velocity structure beneath western Canada and hence provide constraints on the evolution and physical properties of this region. We focus our attention, in particular, on the location of the Cordillera/craton transition and on the northern edge of the Cascadia subduction zone.

2. Data and method

2.1. Data

The traveltime data employed in this study to construct *P*- and *S*-wave velocity models were recorded at stations of the following permanent and temporary networks (see Fig. 1): Advanced National Seismic System (ANSS), Alaska Tsunami Warning System (ATWS), Alaska Regional Network (ARN), BATHOLITHS, CAnadian NOrthwest Experiment (CANOE), Canadian National Seismograph Network (CNSN), and several experiments of the Portable Observatories for Lithospheric Analysis and Research Investigating Seismicity (POLARIS). The *P*-wave data-set consists of 23,420 teleseismic *P* delay times from 1609 earthquakes recorded at 234 broadband and short-period stations at epicentral distances from 30° to 100°. The *S*-wave data-set includes 15,805 teleseismic *S* delay times from 884 events recorded at 194 broadband stations. Azimuthal coverage is good for both data-sets with only one unsampled sector between 200° and 250° (Fig. 2).

Owing to the region's large expanse, source waveforms often exhibit considerable systematic variation between stations at geographic extremes, especially for large earthquakes. Therefore, to facilitate picking *P* and *S* data were divided into independent subsets based on station location. For each subset, *P* and *S* traveltimes were obtained from visual picks of the vertical and transverse component, respectively, which were subsequently refined through multichannel cross-correlation (VanDecar and Crosson, 1990). Frequency bands of 0.4 Hz–1.6 Hz and 0.5 Hz–0.4 Hz were used for *P* and *S* phases, respectively. The timing uncertainty is estimated using the standard deviation of the residual associated with each trace and is on average ~30 ms for *P* and ~120 ms for *S*.

2.2. Model parameterization

The region of interest in this study extends over more than 23° of latitude from 43.5°N to 67.27°N, over 41° of longitude from 105°W to 146°W and from the surface to 700 km depth. For both the *P*- and the *S*-wave inversions the velocity models are parameterized in splines under tension constrained by a series of regularly spaced knots (Fig. 3). The grid is composed of 175,770 knots, 81 in longitude, 70 in latitude and 31 in depth. The dimensions of the smallest elements of the model are 0.33° longitude by 0.5° latitude by 20 km depth, whereas the dimension of the largest elements are 1° longitude by 1° latitude by 25°km. The absolute dimension of the element spacing varies considerably due to the large latitudinal range. The 1D radial earth model IASP91 (Kennett and Engdahl, 1991) was chosen as a reference.

2.3. Traveltime inversion

The traveltime inversion procedure adopted in this study to recover slowness perturbations at every point of our model grid is discussed in detail in VanDecar (1991). This technique produces a solution that represents the minimum variation in seismic velocities required to fit the data by imposing conditions on the first and second spatial derivatives of the model which control the flatness and smoothness, respectively. We chose this form of regularization, as opposed to a more traditional damping, to avoid biasing the solution toward the IASP91 reference which may not necessarily represent a good background model in all portions of the study area.

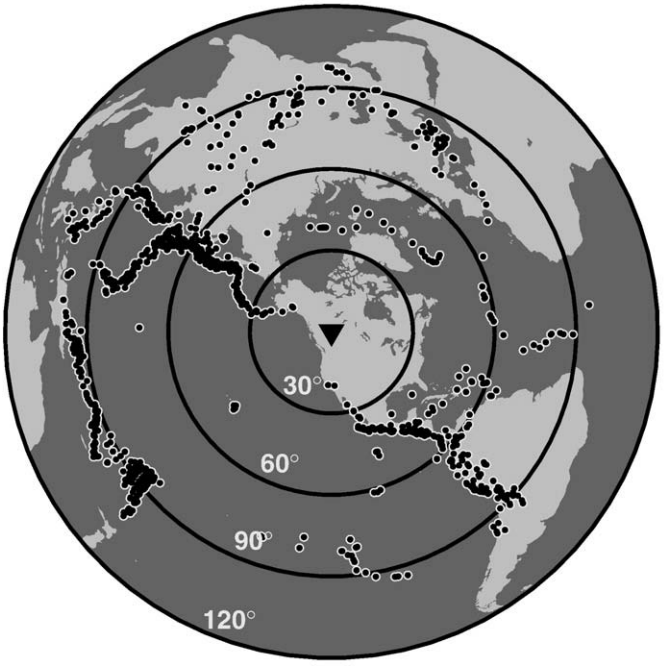

Fig. 2. Equidistant azimuthal projection centered at 55°N and 118°W illustrating the distribution of events with sufficiently high signal-to-noise ratio recorded at one or more stations of the array. Note the relatively uniform azimuthal coverage with only one region between 200° and 250° which is unsampled.

Please cite this article as: Mercier, J.-P., et al., Body-wave tomography of western Canada, Tectonophysics (2009), doi:10.1016/j.tecto.2009.05.030

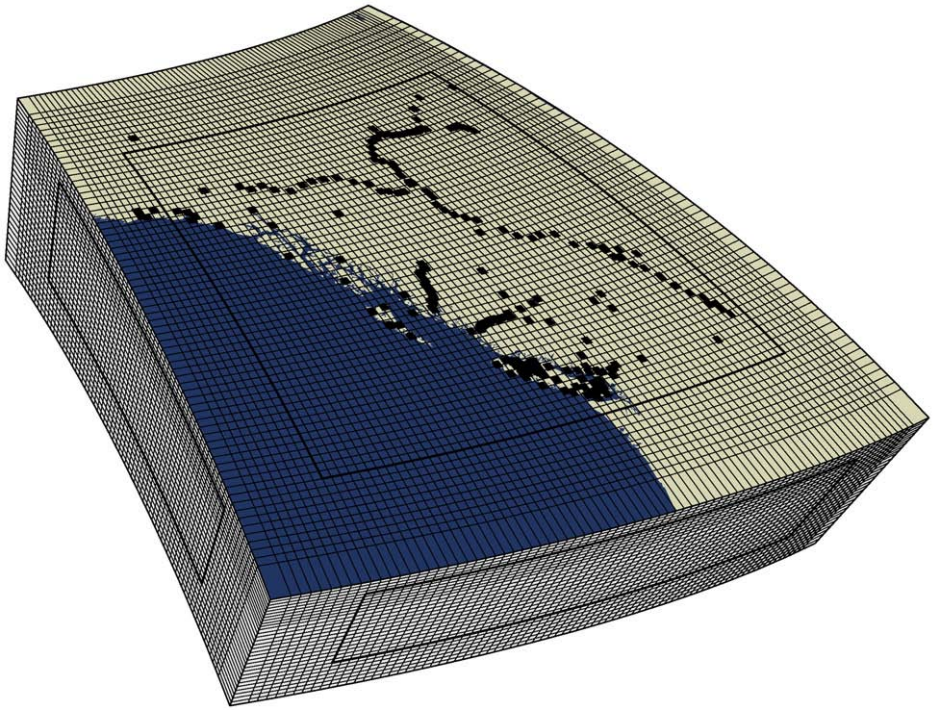

Fig. 3. Three-dimensional view of the grid that constrains the velocity perturbation model with the coast line on top. The velocity model extends from 43.5°N to 67.27°N and 105°W to 146°W, and from the surface to 700 km depth. Knots are positioned at the intersection of the thin black lines. Thick black lines indicate the region to which velocity maps and cross sections are confined. Squares indicate the locations of seismic stations.

The inversion solves the following problem utilizing a combination of conjugate gradient iterations and robust Huber down-weighting (see Huber, 1981):

$$\min_x \Phi_d + \lambda \Phi_m \tag{1}$$

where λ is a free parameter that controls the level of smoothness and flatness of the model, $\Phi_d \overset{\text{def}}{=} \|Ax-b\|^2$, $\Phi_m \overset{\text{def}}{=} \|\Delta\dot{s}\|^2 + \mu\|\Delta\ddot{s}\|^2$. Here, $\Delta\dot{s}$ and $\Delta\ddot{s}$ are vectors containing the first and second derivatives of the slowness perturbations vector at each model point, respectively. The remaining quantities are,

$$A = [P \quad C \quad E], \tag{2}$$

$$x = \begin{bmatrix} \Delta s \\ c \\ e \end{bmatrix} \tag{3}$$

where the matrix P contains the Frechet derivatives which, at knot j and event i, is given by $P_{ij} = \delta t_i / \delta s_j$. Matrices C and E identify stations

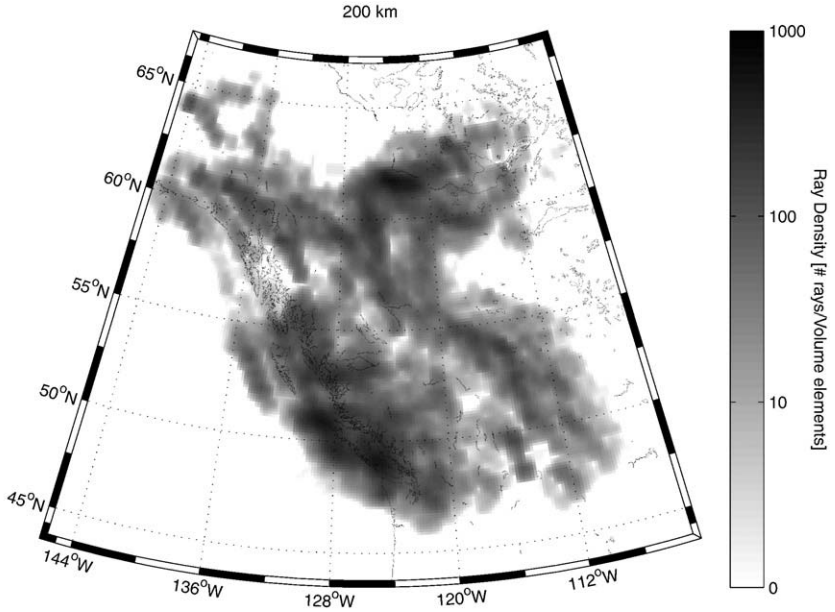

Fig. 4. Ray density map of the region of interest at 200 km depth for the *P* data-set. Black represents the highest density whereas white represents the lowest. Note the logarithmic scale that extends from 0 to 1000 rays. The density is the highest along the three legs of CANOE array and in southwestern British Columbia.

Please cite this article as: Mercier, J.-P., et al., Body-wave tomography of western Canada, Tectonophysics (2009), doi:10.1016/j.tecto.2009.05.030

and events pertaining to a particular traveltime perturbation, respectively; Δs, c, and e are vectors containing the slowness perturbation of every point of the model, the station correction term, and the event correction term respectively; and b is the vector of traveltime residuals. Finally, μ is a free parameter that controls the ratio of smoothness to flatness of the model. It should be noted that the procedure adopted in this study provides good estimates of lateral velocity gradients across a region but does not provide a reliable measure of absolute seismic velocity at a given depth (VanDecar, 1991).

2.4. Choice of inversion parameters

The choice of the regularization parameter λ is a subjective compromise between fitting the data and obtaining a model that is smooth and flat. In this study, we used $\lambda = 350$ and $\mu = 60$ for both *P* and *S* inversions. These values represent a model with slightly greater damping than that represented by the "elbow" of the L-curve. Our selection of this model was based on visual inspection of a large model suite and a desire to present a more conservative estimate of the velocity structure. The number of iterations was determined to ensure convergence to a stable solution. A thousand conjugate gradient iterations within 15 Huber down-weighting iterations were used to produce the *P* model, whereas, due to lower signal-to-noise values of the *S* data-set, 1000 conjugate gradient iterations within 40 Huber down-weighting iterations were required for the *S* inversion.

3. Results

3.1. Resolution test

The ability of the inversion to recover the true *P*- and *S*-velocity models depends both on the ray distribution and the ray geometry (azimuth and incidence angle). Fig. 4 presents the ray density at 200 km depth through the model region. Resolution can be directly assessed using checkerboard resolution tests constructed from synthetic models comprising a succession of positive and negative ellipsoidal anomalies (see Fig. 5). In the test model utilized here, the anomalies are separated by 2° in latitude, 3.5° in longitude and 200 km in depth. The peak velocity anomaly was set to 2% of the background velocity for both *P* and *S* phases.

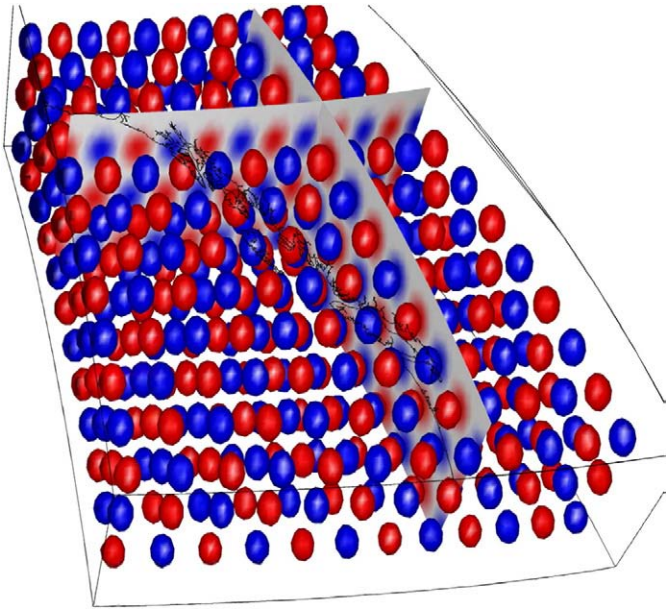

Fig. 5. Input model for the checkerboard resolution test. This model presents alternating positive and negative ellipsoidal velocity perturbations. The red and blue isosurfaces represent a velocity perturbation to the IASP91 reference model of −2% and +2%, respectively.

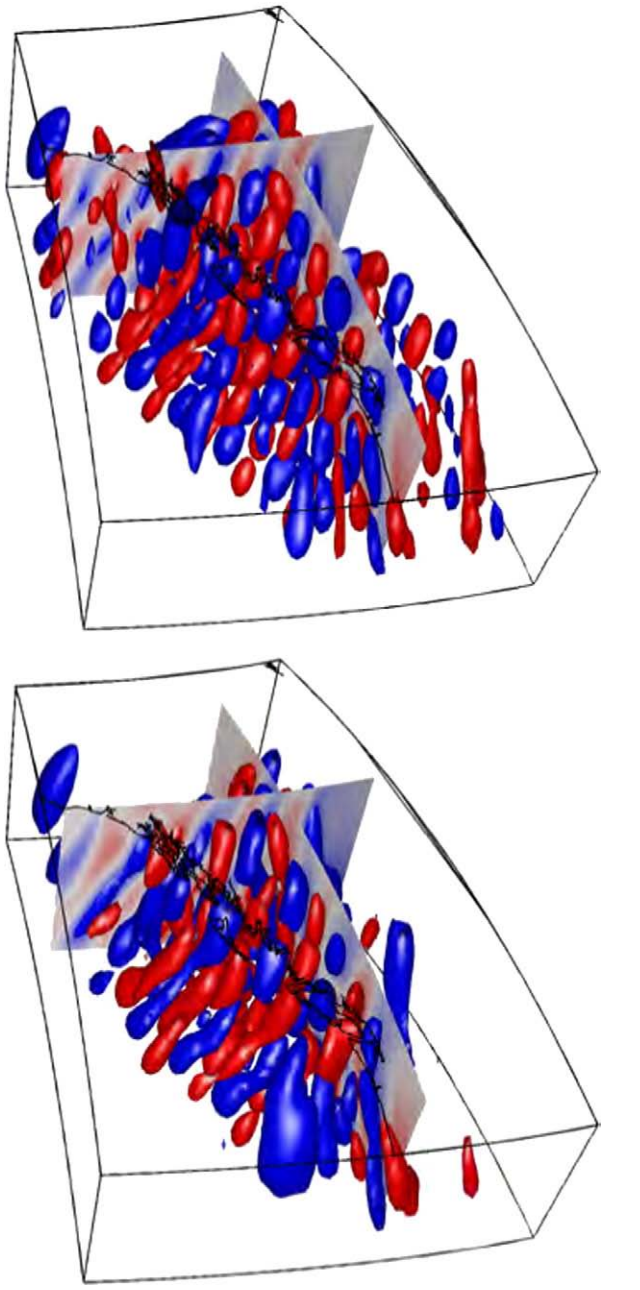

Fig. 6. Result of the resolution test given the input model in 5 for the *P* (top) and *S* (bottom) data-sets. The red and blue isosurfaces represent velocity perturbations of the IASP91 reference model of −1% and +1%, respectively.

Synthetic traveltimes were calculated for these models using the event-station ray geometry of the actual data. Gaussian noise with standard deviations of 30 ms and 200 ms was subsequently added to the *P* and *S* data-sets, respectively. The inversion of the synthetic data-sets was performed using the same procedure and trade-off parameters as employed for the inversion of the real data.

Fig. 6 present the synthetic resolution test results for the *P* and *S* data sets, respectively. The quality of the recovery is variable and depends, as expected, on the local station density. The resolution is best along the CANOE and BATHOLITHS arrays, and in southwestern British Columbia including Vancouver Island, for depths from 100 to 600 km where station coverage is good and ray density is highest for

Please cite this article as: Mercier, J.-P., et al., Body-wave tomography of western Canada, Tectonophysics (2009), doi:10.1016/j.tecto.2009.05.030

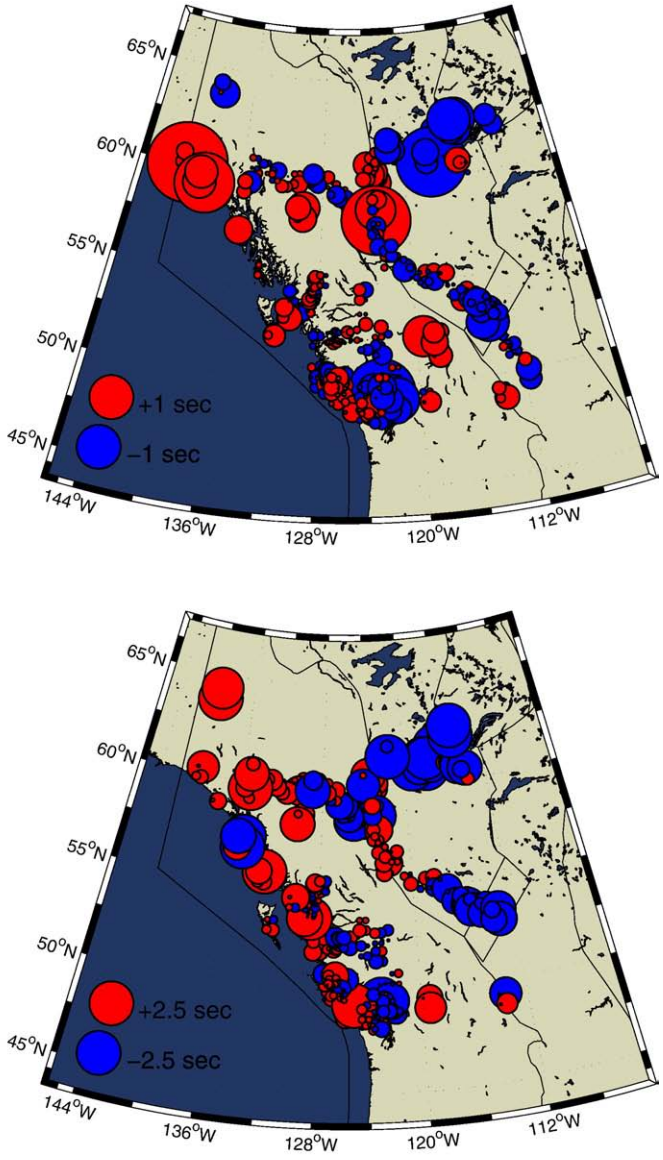

Fig. 7. *P* (top) and *S* wave (bottom) relative station residuals. For each individual station, four residuals are plotted for the north-east, south-east, south-west, and north-west quadrants. Blue and red symbols correspond to early and late arrivals, respectively, with symbol size proportional to the delay.

both *P* and *S* models. Elsewhere, the resolution varies from fair to poor depending on the ray density and station geometry. Overall, where the ray density is greater than 0.1, the correlation coefficients between the original and the recovered models are 0.8 and 0.7 for the *P* and *S* data sets, respectively. Note that the sub-vertical geometry of the teleseismic body-wave raypaths introduces a vertical smearing that reduces resolution in the vertical direction relative to that in the horizontal plane. The recovered velocity anomalies are systematically underestimated and their magnitudes are typically reduced by about 30% compared to the input anomalies. The underestimated amplitudes are a predictable consequence of introducing the station and event correction terms and of the regularization which favors smooth, minimum energy models. Note that Figs. 15–24 present the input and output of the resolution test for results presented in Figs. 8–14.

3.2. Raw average station residuals

Raw residuals provide a good preliminary indication of the velocity structure beneath the study region. Positive residuals indicate the presence of low-velocity structures whereas negative residuals manifest high-velocity anomalies. Fig. 7 combine the average station residuals for the four azimuthal quadrants (northeast, southeast, southwest and northwest) for *P* and *S* phases, respectively. We observe a general agreement between the *P* and *S* values with only few exceptions along the northern segment of the north–south oriented portion of the CANOE array where residual polarities are opposite. Residuals vary considerably within western Canada suggesting fine-scale lateral heterogeneity. Positive residuals are generally observed west of the Cordilleran deformation front whereas negative residuals are observed east of that boundary. Southwestern British Columbia, where most of the mainland stations east of Vancouver Island display negative residuals, remains a notable exception. The few outliers that do not obey these trends are found, however, throughout western Canada, implying small scale complexity in mantle velocity structure.

3.3. P and S upper mantle velocity structure beneath western Canada

Figs. 8 and 9 show 4 horizontal slices through the final *P*- and *S*-velocity models, at depths of 100, 200, 300, and 400 km. Note the good correlation (correlation coefficient of 0.85) between the *P* and *S* images; the similarity between the two models, computed from data sets that are likely largely independent, suggests that the inversions are robust. The RMS reductions for the two data sets are 92% and 81%, respectively. Part of the reduction is absorbed by station corrections which are shown in the 100 km slices.

Two important observations can be taken from the *P* and *S* models. The first is that most of the low-velocity anomalies are observed in the western portion of the study area whereas the east is mostly fast. The transition from low to high-velocity is sharp and well defined at shallow depths, 100 and 200 km, in the south and occurs roughly at the Cordilleran deformation front. North of 55°N the transition becomes less clear due to the presence of a high-velocity anomaly west of the Tintina fault but, nonetheless it appears to correspond to the deformation front. In this area, note that the boundary between low and high-velocity regions tends to dip steeply eastward. The second observation concerns a high-velocity anomaly in south-western British Columbia, east of Vancouver Island. This feature, also eastward dipping, corresponds to the previously documented thermal signature of the Juan de Fuca subducting plate (e.g. VanDecar, 1991; Bostock and VanDecar, 1995). We observe an abrupt termination of the slab signature north of Vancouver Island, near 52°N. The next section will focus specifically on these two regions.

4. Discussion

4.1. Cordillera/craton transition

Precambrian shields are typically underlain by lithospheric roots that are thicker, colder and more depleted in Fe-rich constituents than the young mantle beneath more recent geological formations (Jordan, 1978). The transition from Phanerozoic mantle to cratonic lithosphere is often characterized by a marked change in physical properties that is typically manifest in tomographic models by a sharp increase in seismic velocities. In recent years, several regional and global tomographic studies have provided images of such transitions in various locations around the globe, where young orogens are juxtaposed with cratons (e.g Grand, 1994; Zielhuis and Nolet, 1994; Polet and Anderson, 1995; Ekström et al., 1997; Grand et al., 1997; Simons et al., 1999; Fouch et al., 2004). In western Canada, Frederiksen et al. (2001) and van der lee and Frederiksen (2005) have documented the significant increase in seismic velocity that roughly follows the Cordilleran deformation in the south and Tintina fault in the north.

Please cite this article as: Mercier, J.-P., et al., Body-wave tomography of western Canada, Tectonophysics (2009), doi:10.1016/j.tecto.2009.05.030

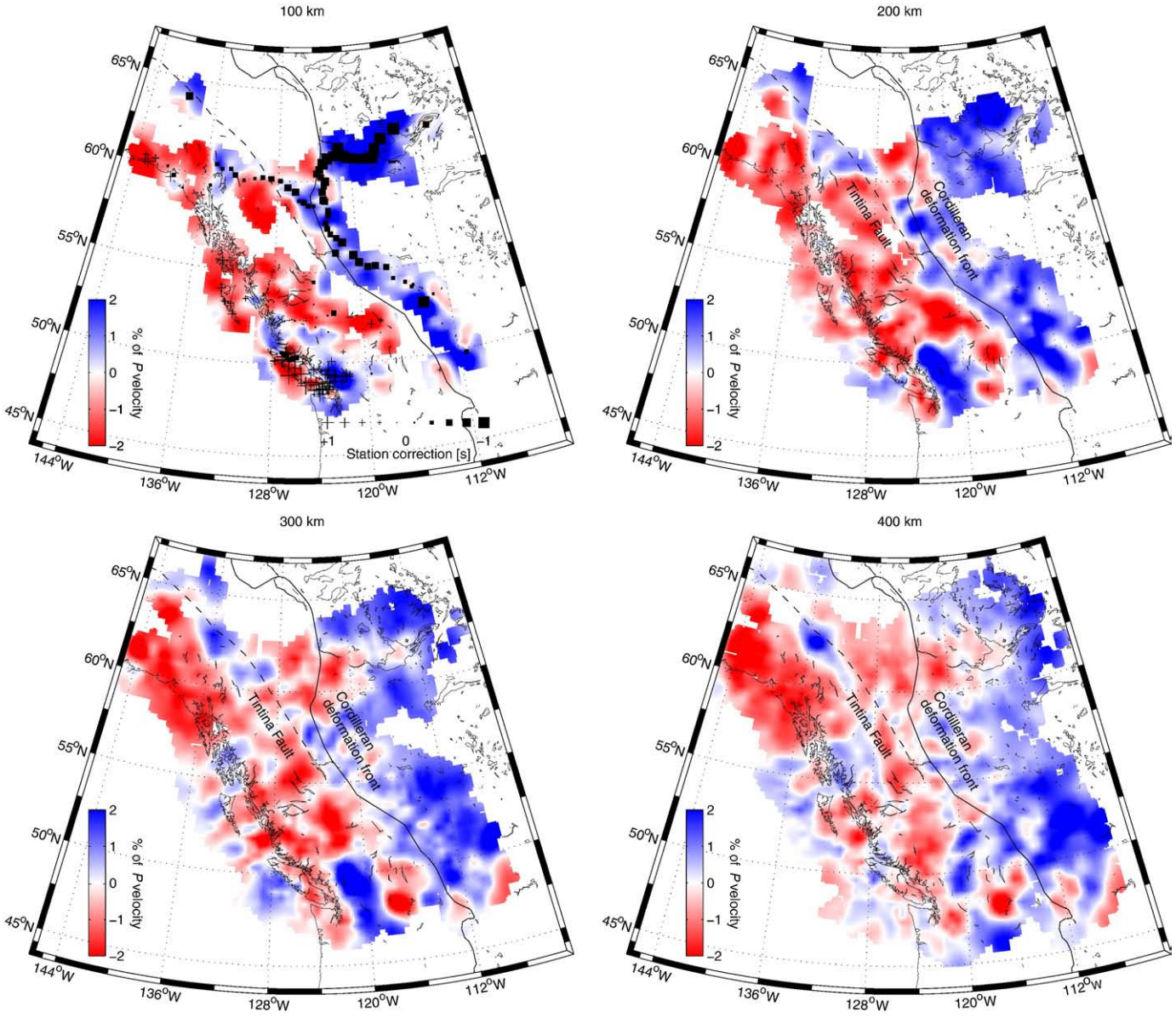

Fig. 8. Depth slices covering the whole survey area at 100 km (top left), 200 km (top right), 300 km (bottom left), and 400 km (bottom right) through the *P* velocity model. This model was obtained from 1000 conjugate gradient iterations within 15 Huber downweightings using $\lambda = 350$ and $\mu = 60$. Blue and red colors represent positive and negative velocity perturbations, respectively. Station corrections are superimposed upon the 100 km model.

There is general consensus that the shift in seismic velocities documented by passive source imaging (Frederiksen et al., 2001; van der lee and Frederiksen, 2005) defines the transition from Phanerozoic mantle to cratonic lithosphere in the south. In the northern Cordillera, however, the situation is more complex. The extension of the western edge of the ancestral North America westward well into the northern Cordillera, as suggested by Frederiksen et al. (1998), Frederiksen et al., (2001), and van der lee and Frederiksen (2005), stands at odds with other geophysical observations. Magnetotelluric (MT) (Jones, 1999; Ledo et al., 2002; Jones et al., 2005) and heat flow data (Hyndman and Lewis, 1999; Lewis et al., 2003), as well as elastic thickness studies (Flück et al., 2003; Audet et al., 2007), suggest instead that the transition occurs roughly at the Cordilleran deformation front. The inferred presence of strong thick and cold cratonic roots beneath the northern Cordillera west of the Tintina fault also poses problems with regard to some basic isostatic considerations (Lachenbruch and Morgan, 1990) and in explaining the origin of the surface deformation which requires a lithosphere that is hot and weak (Hyndman et al., 2005).

The stations deployed along the northern portion of the CANOE array afford an excellent lateral resolution of structure across the northern Cordillera. They are consequently well positioned to locate and characterize the transition from allocthonous to autocthonous mantle in northwestern Canada, in the region where the western extent of the craton is not clearly identified. As mentioned in the previous section, the depth slices in Figs. 8 and 9 indicate that the velocity structure in the northern Cordillera is more complex than in the south. We do image a transition from low to high-velocity west of the Tintina fault, but our results suggest that the major transition in seismic velocity occurs farther east at the Cordilleran deformation front. To better characterize this transition we provide in Fig. 10, a vertical cross section along 60.5°N within the *P*-velocity model, centered on the deformation front, that extends over 15° of longitude. On this figure, three important features are labelled *A*, *B* and *C*.

The structure *A* is a large high-velocity anomaly that extends to depths near 300 km eastward beneath ancestral North America. It is characterized by velocities that are consistently 2%–4% faster than

Please cite this article as: Mercier, J.-P., et al., Body-wave tomography of western Canada, Tectonophysics (2009), doi:10.1016/j.tecto.2009.05.030

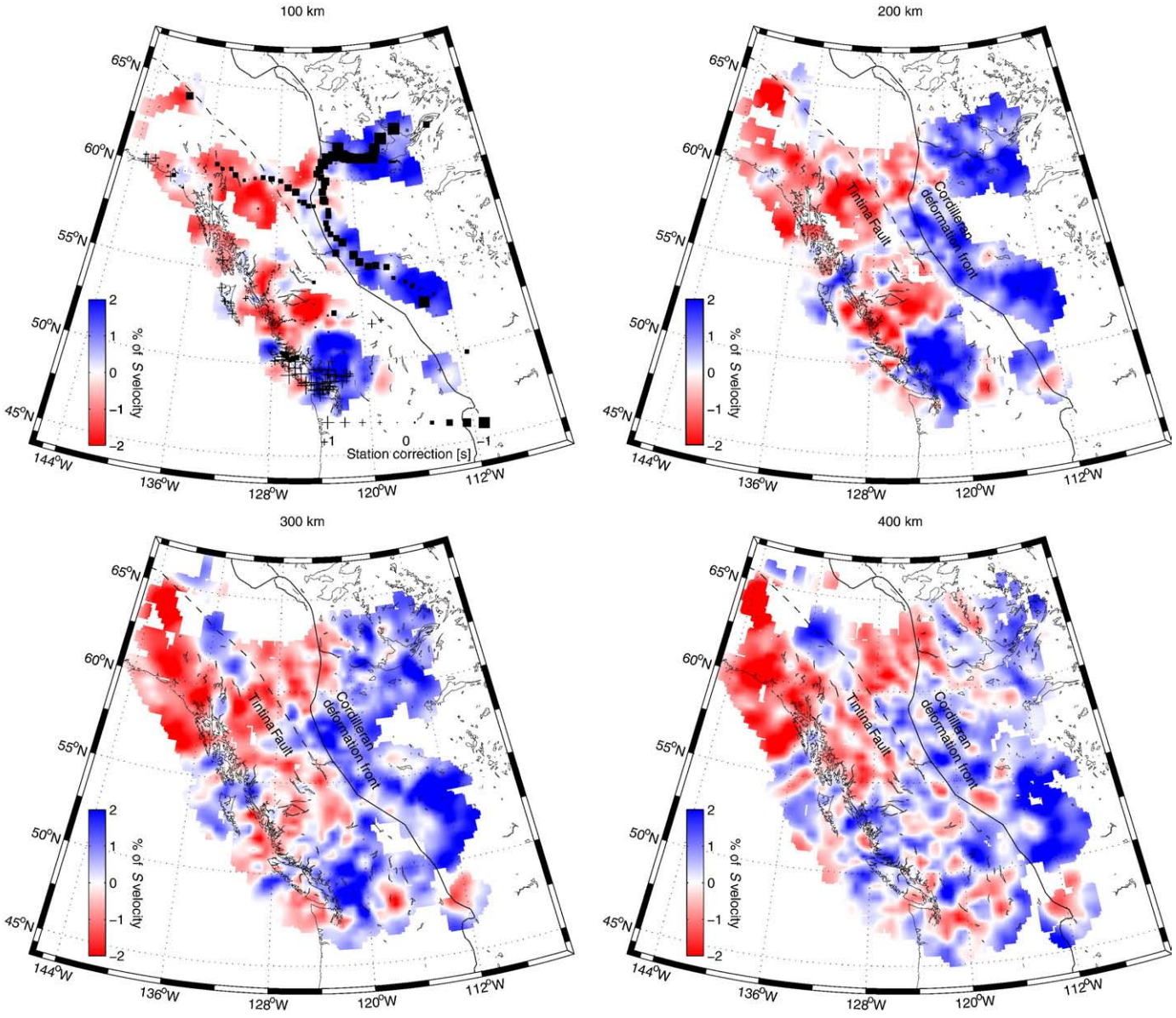

Fig. 9. Depth slices covering the whole survey area at 100 km (top left), 200 km (top right), 300 km (bottom left), and 400 km (bottom right) through the *S* velocity model. This model was obtained from 1000 conjugate gradient iteration within 40 Huber downweightings using a $\lambda = 350$ and $\mu = 60$. Blue and red colors represent positive and negative velocity perturbations, respectively. Station corrections are superimposed upon the 100 km model.

the background value. It is juxtaposed with a low-velocity anomaly of ~ −2% labelled *B* that extends from beneath *A* to the surface. The transition from *A* to *B* is sharp, occurs within less than 50 km and is roughly centered on the Cordilleran deformation front (see Fig. 11). It also coincides with an abrupt variation of surface topography from high to low and with a major change in mantle temperature documented by Hyndman and Lewis (1999) and Lewis et al. (2003) from heat flow measurements, and to a lesser extent by Flück et al. (2003) and Audet et al. (2008) from the study of elastic thickness. This combination of observations strongly suggests that the transition from *B* to *A* corresponds to the boundary between Phanerozoic mantle and Proterozoic lithosphere, thereby shifting the western extent of the craton by hundreds of kilometers eastward from what was proposed by Frederiksen et al. (1998), and Frederiksen et al. (2001) and van der lee and Frederiksen (2005) using body-wave or surface-wave tomography, respectively.

The discrepancy in location of the Phanerozoic/craton boundary in northwestern Canada with some previous studies can be attributed to the presence of a mostly high-velocity anomaly identified by *C* that extends over 400 km west of Tintina fault and displays localized variations in velocities under ±2%. Although we are unable to offer a specific explanation for *C*, the Tintina Fault is recognized as a major strike–slip boundary (Price and Carmichael, 1986) along which seismically distinct Phanerozoic mantle lithospheres may have been juxtaposed. Some previous studies, lacking either the resolution or broader geographical context of the present work may thus have misinterpreted this feature as the craton boundary.

The results presented here position the boundary between Phanerozoic and cratonic mantle at the Cordilleran deformation front in northwestern Canada and are consistent with the aforementioned heat flow and gravity observations. This is not surprising since coincident velocity transitions from high to low topography and from hot Proterozoic to cold Precambrian mantle have been observed in many other instances across the globe (e.g. Australia (Simons et al., 1999), United States (Dueker et al., 2001), and Northern Europe (Zielhuis and Nolet, 1994)).

Please cite this article as: Mercier, J.-P., et al., Body-wave tomography of western Canada, Tectonophysics (2009), doi:10.1016/j.tecto.2009.05.030

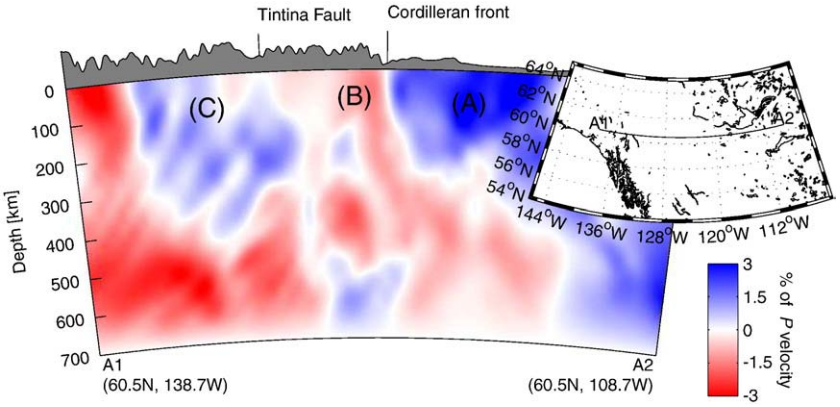

Fig. 10. Cross section within the *P* velocity model along the corridor A1–A2 (see inset map at top right) in the northern Cordillera from the surface to a depth of 600 km. The topography plotted on top of the cross section is exaggerated 50 times and smoothed. Blue and red represent positive and negative velocity perturbations, respectively.

4.2. Subsurface geometry of Northern Cascadia

The northern Cascadia subduction zone is a complex tectonic environment characterized by the transition from convergent to transform boundary that involves interaction between the North American continent and three oceanic plates, namely the Juan de Fuca (JdF), Explorer (EXP), and Pacific plates (PAC) (see tectonic setting in Fig. 12). Although, the structure of Cascadia has been extensively studied in its southern and central portions, its northernmost section remains relatively unexplored due to a historical shortage of geophysical observations in general and seismic data in particular. The geometry of its subsurface is only loosely constrained by scattered heat flow, gravity and geochemical data (Lewis et al., 1997). The recent deployment of broadband three-component seismic stations on northern Vancouver Island, the Nechako area of central British Columbia and along the two arms of the BATHOLITHS array, now permits the study of subsurface structures at the northern edge of the subducting Juan de Fuca plate system and mantle to the north.

4.2.1. Juan de Fuca slab and convergence north of Cascadia Subduction Zone

The structure of the northern Cascadia region from 48.5°N up to 50°N has been investigated previously by Bostock and VanDecar (1995) using traveltime tomography. Their velocity model features a quasi-planar, high-velocity body inferred to represent the thermal and compositional anomaly of the subducted Juan de Fuca plate. This body exhibits velocity deviations of up to 3% from the background reference model and extends to depths of at least 400–500 km. Cassidy et al. (1998), using five seismic stations deployed in Northern Vancouver Island and on the adjacent mainland, provided constraints on the shallow *S* wave velocity structure in Northern Vancouver Island. They observed a pronounced change in the *S* velocity structure that was interpreted as the northern limit of the subducted oceanic plate beneath Vancouver Island. Using considerably more seismic stations (26 vs 5) Audet et al. (2008) focused on the structure of the subducted Explorer plate beneath the same region. Based on receiver function and tomography results, these authors proposed a tectonic model in which the separation of the Explorer plate from the Juan de Fuca plate

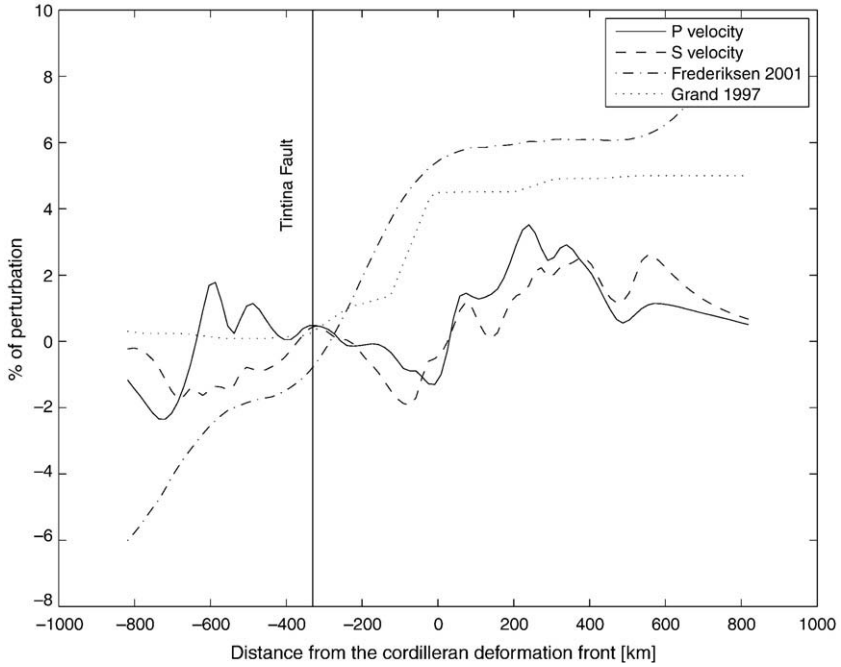

Fig. 11. Plot of the velocity variation at 100 km depth along A1–A2 (see Fig. 10) centered on the Cordillera deformation front. Plain line represents the *P* velocity perturbations, dashed line the *S* perturbations, dashed/dotted line the (Frederiksen et al., 2001) model, and dashed line (Grand et al., 1997).

Please cite this article as: Mercier, J.-P., et al., Body-wave tomography of western Canada, Tectonophysics (2009), doi:10.1016/j.tecto.2009.05.030

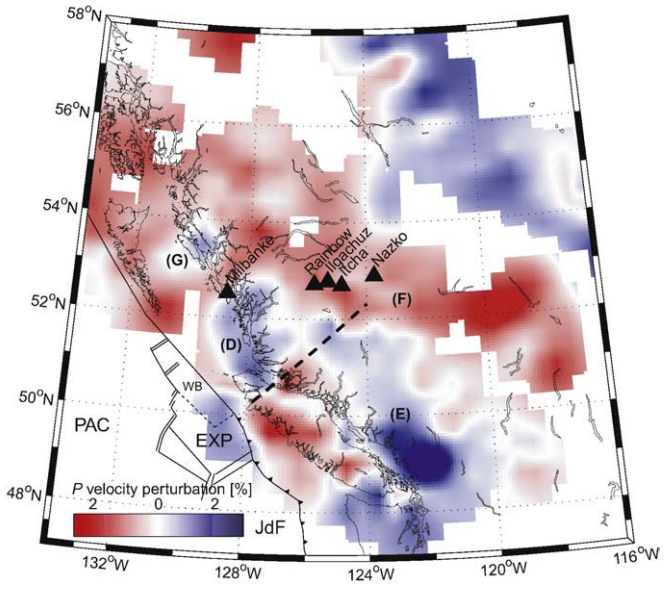

Fig. 12. Depth slice at 100 km depth within the *P* velocity model in southwestern British Columbia with tectonics of northern Cascadia detailed. Blue and red represent, again, positive and negative velocity perturbations, respectively. Triangles represent locations of volcanic centers.

is described as the consequence of thermo-mechanical erosion of the slab edge and slab thinning at shallow levels and where the slow convergence of the Explorer plate with North America will eventually lead to its capture by the Pacific plate. Bostock and VanDecar (1995), Cassidy et al. (1998), and Audet et al. (2008) did not, however, explore the region beyond the northern tip of Vancouver Island.

Fig. 12 presents an expanded view of the *P*-velocity model along the British Columbia coast at a depth of 100 km. On this figure, four features are identified as *D*, *E*, *F*, and *G*. The structure *D* represents a high-velocity anomaly that lies south-east of the Queen Charlotte Islands. It may represent the subducted downdip portion of oceanic lithosphere, formerly part the Pacific plate, that detached from the slab during the formation of the Winona block (WB) at ~1 Ma (Davis and Riddihough, 1982). The high-velocity anomaly *E* is easier to interpret and represents the previously documented thermal and compositional signature of the Juan de Fuca slab (Bostock and VanDecar, 1995). The signature of the slab represents a velocity anomaly of ~3% in the south and less than 2% in the north. Inland, its northwestern terminus coincides roughly with the projection of the Juan de Fuca displacement vector of the interpreted slab edge beneath Vancouver island documented by Lewis et al. (1997), Cassidy et al. (1998), and Audet et al. (2008) (see dashed line on Fig. 12). As we elaborate upon below, the low-velocity anomaly identified by *F* is visible beneath part of the northern Cordillera and may be the expression of the slab gap that formed at 45 Ma as a result of the cessation of the subduction of the Kula/Resurrection plate along the northern Canadian margin (presently Queen Charlotte fault). *G* is a relatively small high-velocity anomaly located east of the Queen Charlotte Basin that may represent the signature of the Pacific plate.

The slices A1–A2 and B1–B2 in Fig. 13, present two cross sections perpendicular to the strike of Juan de Fuca subduction. On both images, we observe a north-eastward dipping high-velocity anomaly up to 3% that represents the signature of the subducting Juan de Fuca slab. In the south, cross section (A1–A2), the geometry of the slab is well defined and continuous. It dips at a ~60° angle and is traceable to a depth of at least 400–500 km although some smearing may be present. This result is in agreement with the findings of Bostock and VanDecar (1995). In the north, the anomaly is not as clearly delineated and is only defined to depths of ~300 km. It dips, however, at a similar angle. The degradation of the slab signature northward may be attributed to the lower station density over this region, or alternatively, could result from the action of the erosion mechanisms at the northern edge of the subducting plate.

From the cross section C1–C2 of Fig. 13, we observe the signature of a dipping structure that may reflect plate convergence north of the Cascadia subduction zone. This north-eastward dipping anomaly represents a 2% perturbation that is evident to a depth ~200 km. As discussed previously, it may represent the signature formerly subducting material that detached from the Pacific plate, 1 Ma ago, during the formation of the Winona block. It is less clear however, whether there is convergence farther north along the Queen Charlotte Fault. The Queen Charlotte Fault is known to be principally a transform boundary that accommodates ~50 mm/a of strike–slip motion. It also contains, however, a significant component (~15 mm/a) of convergence across the margin e.g. DeMets and Dixon (1999), Kreemer et al. (2003), Mazzotti et al., (2003). Two models have been proposed to accommodate the ~15 mm/a of convergence. The first model involves deformation and shortening within the Queen Charlotte Basin and the Pacific and North American plates e.g. Rohr et al., (2000). The second model involves underthrusting of a Pacific slab beneath the North American Plate e.g. (Yorath and Hyndman, 1983; Hyndman and Hamilton, 1993; Bustin et al., 2007). The presence of a high-velocity anomaly centered at 53.5 N, 130 W, labelled *G*, within our velocity model may suggest that convergence exists. However, on the cross section D1–D2 of Fig. 13, this anomaly does not share the dipping geometry of the subducting slabs evident in the south (i.e. feature *D* and *F*).

4.2.2. Anahim volcanic belt and the Chilcotin group

We now turn our attention to the southern edge of the low-velocity zone *F*, just north of the subducting plate identified by *E* shown in Fig. 12. In this region, upper Miocene–Quaternary alkalic and peralkalic volcanism is observed along the Anahim volcanic belt and within the Chilcotin plateau basalts, alternatively referred to as the Chilcotin group, contrasting with the subduction driven calc-alkalic volcanism found in the nearby Pemberton and Garibaldi volcanic belt (Bevier, 1989). The Anahim volcanic belt is a 600 km long west–east trending chain of volcanoes that began to erupt at ~14.5 Ma near the coast and progressed inland to the east, at a rate that varies from 20 to 33 mm/a (Bevier et al., 1979). This belt is composed of four major volcanic centers: The Milbanke Sound group (52.5°N 128.7°W, ~14.5 Ma), the Rainbow Range (52.7°N 125.8°W, ~8 Ma), the Ilgachuz Range (52.8°N 125.3°W, ~5 Ma), the Itcha Range (52.7°N 124.9°W, ~2.5 Ma) and the Nazko Range (52.9°N, 123.7°W, 0.01–0.34 Ma) which is the site of more recent volcanic (Bevier et al., 1979) and seismic activity. Magmatism in the Chilcotin Plateau Basalts, spanned about 16 million years, and occurred in the same area during three main episodes: 15–13 Ma, 9–6 Ma, and 3–1 Ma (Bevier, 1983b; Mathews, 1989). Although possibly coincidental, the appearance of volcanic activity in the Anahim belt and Chilcotin group at ~15 Ma also coincides with an acceleration of uplift rate in the central Coast Mountains (53°–54°), from 0.1–0.2 km/Ma to 0.4 km/Ma (Parrish, 1983).

Several mechanisms have been proposed to explain the origin of magmatism in this region. Rohr and Currie (1997) suggested that simple lithospheric-scale shear could account simultaneously for the subsidence of the Queen Charlotte Basin, the uplift of the central Coast mountains, and the Neogene basalt flow and plutonism in the Anahim belt and Chilcotin group. Asthenospheric flow along the northern edge of the subducting slab was also hypothesized as a plausible cause for the magmatism (Stacey, 1974; Souther et al., 1987). The presence of a mantle plume has also been invoked as a potential source of magmatism (Bevier, 1983a; Souther et al., 1987). This idea is supported by the observation that the 20–30 mm/a eastward migration of volcanism in the Anahim belt compares well with the 27 mm/a of the Yellowstone (Wyoming) and Raton hotspots (New Mexico), and is consistent with the predicted 25.1 mm/a rate of movement of the North American plate at the center of the volcanic

Please cite this article as: Mercier, J.-P., et al., Body-wave tomography of western Canada, Tectonophysics (2009), doi:10.1016/j.tecto.2009.05.030

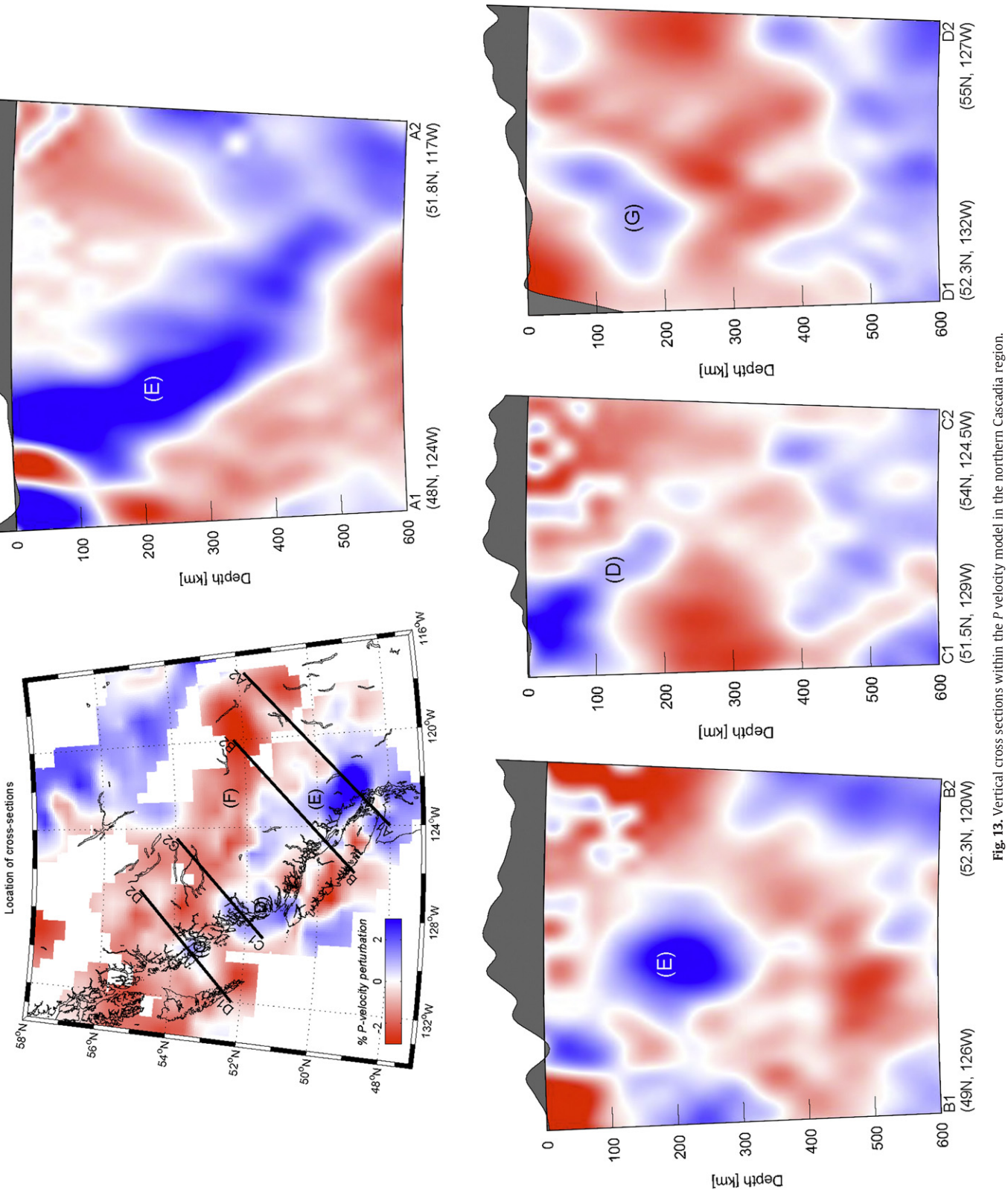

Fig. 13. Vertical cross sections within the *P* velocity model in the northern Cascadia region.

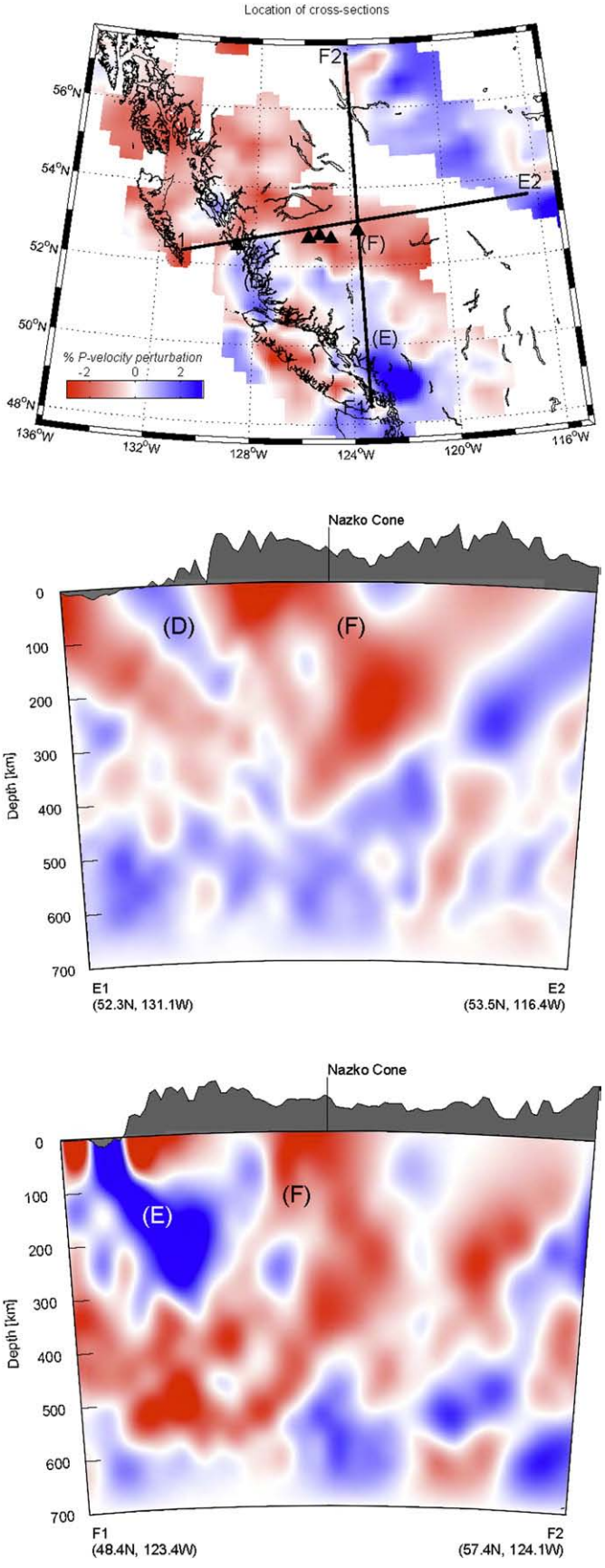

Fig. 14. Vertical cross sections within the *P* velocity model.

belt (52°N, 125°W) (Minster et al., 1974). The peralkalic composition of the Anahim and Chilcotin basalts are also consistent with the plume origin (Bevier, 1989).

Fig. 14 presents cross sections parallel (E1–E2) and perpendicular (F1–F2) to the inferred hotspot track. On the north–south cross section (F1–F2), we observe that the low-velocity anomaly is centered near Nazko Cone and extends to a depth of ~400 km. The~−2% anomaly is flanked on both sides by high-velocity anomalies of variable amplitude. In the south, we recognize the signature of the Juan de Fuca subducting slab complex. High velocities in the north may reflect the remnant of batholithic roots that formed as a result of continuous subduction along the northern margin from ~150 Ma to ~50 Ma. On the west–east cross section (E1–E2), the low-velocity anomaly extends from the current location of the Anahim hotspot at Nazko cone seaward along the hotspot track. East of Nazko cone, we observe a small high-velocity anomaly marking the eastern extent of the hotspot track. In the west, we recognize the signature of the high-velocity anomaly labelled *D* in Fig. 12. From the images in Fig. 14, we observe that the low-velocity anomaly is visible to a depth of ~400 km directly beneath Nazko Cone. As suggested by our model, the low-velocity anomaly may, however, extend deeper southward beneath the Juan de Fuca plate.

Low-velocity anomalies extending beneath hotspots, or hotspot tracks have been imaged by regional traveltime tomography in several other locations around the globe e.g. Hawaii (Ellsworth and Koyanagi, 1977; Tilmann, 1999), Yellowstone (Iyer et al., 1981; Evans, 1982; Saltzer and Humphreys, 1997), the Massif Central (Granet et al., 1995), Iceland (Wolfe et al., 1997), and in Germany (Ritter et al., 2001). The general consensus is that these anomalies are related to or are the source of volcanism observed at the surface. By analogy, the presence in our tomographic model of a low-velocity anomaly present beneath Nazko Cone that extends seaward along the Anahim volcanic track suggests a direct relation to the magmatism observed in this region. Our results, consequently, support models of volcanism that involve mantle-scale rather that lithosphere-scale processes (i.e. simple lithospheric-scale shear Rohr and Currie, (1997), but cannot distinguish between asthenospheric flow along the slab edge (Stacey, 1974; Souther et al., 1987) and mantle plume models (Bevier, 1983a; Souther et al., 1987)).

Upwelling of asthenosphere along the slab edge is postulated to exist in slab window environments where a pair of diverging plate is subducted beneath a continent (e.g. Dickinson and Snyder, 1979; Johnson and O'Neil, 1984; Forsythe and Nelson, 1985; Thorkelson and Taylor, 1989; Thorkelson, 1996). This concept could perhaps be applied to the current tectonic setting where the gap left north of the Juan de Fuca plate, following the end of subduction along what is now the Queen Charlotte Fault, may have focussed upwelling asthenosphere toward the Anahim volcanic belt region. Shear-wave splitting observations in the southern Cascadia region are suggestive of such complex flow along the edge of subducting plates (Zandt and Humphreys, 2008). The sudden appearance of magmatism at ~15 Ma and the steady spatio-temporal eastward progression of the hotspot along an axis coherent with the displacement of the North American plate are, however, less readily accounted for by this model. The obliquity of the Juan de Fuca plate motion to the hotspot track also poses a geometrical problem. The presence of a mantle plume either confined to the upper-mantle, or extending beneath the subducting plate below the transition zone offers a simpler explanation. Mantle plumes are known to be stable to convection over an extended period of time (e.g. Nataf, 2000) and are recognized to be the source of hotspot volcanism and perhaps also the source of flood basalts in several similar locations (Richards et al., 1989; Duncan and Richards, 1991).

5. Conclusion

In this paper, we have presented the first regional-scale, high resolution *P* and *S* velocity models across western Canada, utilizing

Please cite this article as: Mercier, J.-P., et al., Body-wave tomography of western Canada, Tectonophysics (2009), doi:10.1016/j.tecto.2009.05.030

data collected at stations from a variety of temporary and permanent seismic networks. Our models indicate that the western portion of the study area displays a generally lower velocity, whereas the eastern region is mostly fast. The only significant exception is the presence of a broad high-velocity anomaly in the Cascadia subduction zone. In this study we focused our attention on two areas where our station distribution affords the best resolution, namely, the corridor along legs A and B of the CANOE array in Northwestern Canada, and the northern margin of Cascadia where the plate boundary changes from convergent to transform. In northwestern Canada, we have characterized the transition from Cordilleran to cratonic mantle. We argue that the main change occurs at the Cordilleran deformation front and represents a sharp increase in mantle seismic velocity greater than 4% over a distance of ~50 km. At the northern margin of Cascadia, we have imaged three significant velocity anomalies: a high-velocity anomaly centered at 51°N, 128°W, dipping eastward, possibly representing the remnant of the slowly converging Winona block; a high-velocity anomaly representing the thermal signature of the Juan de Fuca subducting plate; and a low-velocity anomaly north of the slab. Immediately north of the northern edge of the slab, we have paid special attention to mantle structure along and perpendicular to the Anahim hotspot track. In this region, our model reveals a low-velocity zone north of the Juan de Fuca plate that extends well into mantle depth beneath Nazko Cone and may continue southward beneath the Juan de Fuca plate. Our observations suggest that a deep-seated low-velocity anomaly is the source of magmatism in the Anahim volcanic belt and Chilcotin Basalt group, and, consequently, that a mantle-scale process rather than lithospheric scale process controls surface volcanism. Coupled with the well documented temporal progression of surface volcanism, our model favors an origin for the hotspot track in the form of a mantle plume over slab edge flow.

Appendix A. Supplementary data

Supplementary data associated with this article can be found, in the online version, at doi:10.1016/j.tecto.2009.05.030.

References

Audet, P., Bostock, M.G., Mercier, J.-P., Cassidy, J.F., 2008. Morphology of the Explorer-Juan de Fuca slab edge in northern Cascadia: imaging plate capture at a ridge-trench-transform triple junction. Geology 36, 895–898.

Audet, P., Jellinek, A.M., Uno, H., 2007. Mechanical controls on the deformation of continents at convergent margins. Earth Planet. Sc. Lett. 264, 151–166.

Bevier, M., 1983a. Implications of chemical and isotopic composition for petrogenesis of Chilcotin Group basalts, British Columbia. J. Petrol. 24, 207–226.

Bevier, M., 1983b. Regional stratigraphy and age of Chilcotin Group basalts, south-central British Columbia. Can. J. Earth Sci. 20, 515–524.

Bevier, M., Armstrong, R., Souther, J., 1979. Miocene peralkaline volcanism in West-central British Columbia; its temporal and plate-tectonics setting. Geology 7, 389–392.

Bevier, M.L., 1989. A lead and strontium isotopic study of the Anahim volcanic belt, British Columbia; additional evidence for widespread suboceanic mantle beneath western North America. Geol. Soc. Am. Bull. 101, 973–981.

Bostock, M.G., VanDecar, J.C., 1995. Upper-mantle structure of the northern cascadia subduction zone. Can. J. Earth Sci. 32, 1–12.

Buchbinder, G., Poupinet, G., 1977. P-wave residuals in Canada. Can. J. Earth Sci. 14, 1292–1304.

Bustin, A., Hyndman, R., Kao, H., Cassidy, J., 2007. Evidence for underthrusting beneath the Queen Charlotte Margin, British Columbia, from teleseismic receiver function analysis. Geophys. J. Int. 171, 1198–1211.

Cassidy, J., Ellis, R., Karavas, C., Rogers, G., 1998. The northern limit of the subducted Juan de Fuca plate system. J. Geophys. Res. 103, 26949–26961.

Davis, E., Riddihough, R., 1982. The Winona Basin: structure and tectonics. Can. J. Earth Sci. 19, 767–788.

DeMets, C., Dixon, T., 1999. New kinematic models for Pacific–North America motion from 3 Ma to present, I: evidence for steady motion and biases in the NUVEL-1A model. Geophys. Res. Lett. 26, 1921–1924.

Dickinson, W., Snyder, W., 1979. Geometry of subducted slabs related to San Andreas transform. J. Geol. 87, 609–627.

Dueker, K., Yuan, H., Zurek, B., 2001. Thick-structured Proterozoic lithosphere of the Rocky Mountain Region. GSA Today 11, 4–9.

Duncan, R., Richards, M., 1991. Hotspots, mantle plumes, flood basalts, and true polar wander. Rev. Geophys. 29, 31–50.

Ekström, G., Tromp, J., Larson, E., 1997. Measurements and global models of surface wave propagation. J. Geophys. Res. 102, 8137–8158.

Ellsworth, W., Koyanagi, R., 1977. Three-dimensional crust and mantle structure of Kilauea Volcano, Hawaii. J. Geophys. Res. 82, 5379–5394.

Evans, J., 1982. Compressional wave velocity structure of the upper 350 km under the eastern Snake River Plain near Rexburg, Idaho. J. Geophys. Res. 87, 2654–2670.

Flück, P., Hyndman, R., Lowe, C., 2003. Effective elastic thickness Te of the lithosphere in western Canada. J. Geophys. Res. 108. doi:10.1029/2002JB002201.

Forsythe, R., Nelson, E., 1985. Geological manifestations of ridge collision: evidence from the Golfo de Penas–Taitao Basin, southern Chile. Tectonics 4, 477–495.

Fouch, M., James, D., VanDecar, J., van der Lee, S., 2004. Mantle seismic structure beneath the Kaapvaal and Zimbabwe Cratons. S. Afr. J. Geol. 107, 33–44.

Frederiksen, A.W., Bostock, M.G., Cassidy, J.F., 2001. S-wave velocity structure of the Canadian upper mantle. Phys. Earth Planet. In. 124, 175–191.

Frederiksen, A.W., Bostock, M.G., VanDecar, J.C., Cassidy, J.F., 1998. Seismic structure of the upper mantle beneath the northern Canadian Cordillera from teleseismic travel-time inversion. Tectonophysics 294, 43–55.

Grand, S., van der Hilst, R.D., Widiyantoro, S., 1997. High resolution global tomography: a snapshot of convection in the Earth. GSA Today 7, 1–7.

Grand, S.P., 1994. Mantle shear structure beneath the America and surrounding oceans. J. Geophys. Res. 99, 11591–11621.

Granet, M., Wilson, M., Achauer, U., 1995. Imaging a mantle plume beneath the French Massif Central. Earth Planet. Sci. Lett. 136, 281–296.

Huber, P., 1981. Robust Statistics.

Humphreys, E.D., Dueker, K.G., 1994. Western United-States upper-mantle structure. J. Geophys. Res. 99, 9615–9634.

Hyndman, R., Currie, C., Mazzotti, S., 2005. Subduction zone backarcs, mobile belts, and orogenic heat. GSA Today 15, 4–10.

Hyndman, R., Hamilton, T., 1993. Queen Charlotte area Cenozoic tectonics and volcanism and their association with relative plate motions along the northeastern Pacific margin. J. Geophys. Res. 98, 14257–14277.

Hyndman, R., Lewis, T., 1999. Geophysical consequences of the Cordillera–Craton thermal transition in southwestern Canada. Tectonophysics 306, 397–422.

Iyer, H.M., Evans, J.R., Zandt, G., Stewart, R.M., Coakley, J.M., Roloff, J.N., 1981. A deep low-velocity body under the Yellowstone caldera, Wyoming: delineation using teleseismic P-wave residuals and tectonic interpretation: summary. B. Seismol. Soc. Am. 92, 792–798.

Johnson, C., O'Neil, J., 1984. Triple junction magmatism: a geochemical study of Neogene volcanic rocks in western California. Earth Planet. Sci. Lett. 71, 241–262.

Jones, A., 1999. Imaging the continental upper mantle using electromagnetic methods. Lithos 48, 57–80.

Jones, A., Ledo, J., Ferguson, I., Farquharson, C., Garcia, X., Grant, N., McNeice, G., Roberts, B., Spratt, J., Wennberg, G., et al., 2005. The electrical resistivity structure of Archean to Tertiary lithosphere along 3200 km of SNORCLE profiles, northwestern Canada. Can. J. Earth Sci. 42, 1257–1275.

Jordan, T., 1978. Composition and development of the continental tectosphere. Nature 274, 544–548.

Kennett, B.L.N., Engdahl, E.R., 1991. Traveltimes for global earthquake location and phase identification. Geophys. J. Int. 105, 429–465.

Kreemer, C., Holt, W., Haines, A., 2003. An integrated global model of present-day plate motions and plate boundary deformation. Geophys. J. Int. 154, 8–34.

Lachenbruch, A., Morgan, P., 1990. Continental extension, magmatism and elevation; formal relations and rules of thumb. Tectonophysics 174, 39–62.

Ledo, J., Jones, A., Ferguson, I., 2002. Electromagnetic images of a strike–slip fault—the Tintina Fault Northern Canadian. Geophys. Res. Lett. 29. doi:10.1029/2001GL013408.

Lewis, T., Hyndman, R., Flück, P., 2003. Heat flow, heat generation, and crustal temperatures in the northern Canadian Cordillera: thermal control of tectonics. J. Geophys. Res. 108. doi:10.1029/2002JB002090.

Lewis, T., Lowe, C., Hamilton, T., 1997. Continental signature of a ridge–trench-triple junction: Northern Vancouver Island. J. Geophys. Res. 102, 7767–7781.

Mathews, W., 1989. Neogene Chilcotin basalts in south-central British Columbia: geology, ages, and geomorphic history. Can. J. Earth Sci. 26, 969–982.

Mazzotti, S., Dragert, H., Henton, J., Schmidt, M., Hyndman, R., James, T., Lu, Y., Craymer, M., 2003. Current tectonics of northern Cascadia from a decade of GPS measurements. J. Geophys. Res 108. doi:10.1029/2003JB002653.

Minster, J., Jordan, T., Molnar, P., Haines, E., 1974. Numerical modelling of instantaneous plate tectonics. Geophys. J. Int. 36, 541–576.

Nataf, H., 2000. Seismic imaging of mantle plumes. Annu. Rev. Earth. Planet. Sci. 28, 391–417.

Parrish, R., 1983. Cenozoic thermal evolution and tectonics of the Coast Mountains of British Columbia 1. Fission track dating, apparent uplift rates, and patterns of uplift. Tectonics 2, 601–632.

Polet, J., Anderson, D., 1995. Depth extent of cratons as inferred from tomographic studies. Geology 23, 205–208.

Price, R., Carmichael, D., 1986. Geometric test for Late Cretaceous–Paleogene intracontinental transform faulting in the Canadian Cordillera. Geology 14, 468–471.

Richards, M., Duncan, R., Courtillot, V., 1989. Flood basalts and hot-spot tracks: plume heads and tails. Science 246, 103–107.

Ritter, J., Jordan, M., Christensen, U., Achauer, U., 2001. A mantle plume below the Eifel volcanic fields, Germany. Earth Planet. Sci. Lett. 186, 7–14.

Rohr, K., Currie, L., 1997. Queen Charlotte Basin and Coast Mountains; paired belts of subsidence and uplift caused by a low-angle normal fault. Geology 25, 819–822.

Rohr, K.M.M., Scheidhauer, M., Trehu, A.M., 2000. Transpression between two warm mafic plates: the Queen Charlotte Fault revisited. J. Geophys. Res. 105, 8147–8172.

Saltzer, R., Humphreys, E., 1997. Upper mantle *P* wave velocity structure of the eastern Snake River Plain and its relationship to geodynamic models of the region. J. Geophys. Res. 102, 11829–11842.

Shragge, J., Bostock, M.G., Bank, C.G., Ellis, R.M., 2002. Integrated teleseismic studies of the southern Alberta upper mantle. Can. J. Earth Sci. 39, 399–411.

Please cite this article as: Mercier, J.-P., et al., Body-wave tomography of western Canada, Tectonophysics (2009), doi:10.1016/j.tecto.2009.05.030

Simons, F., Zielhuis, A., van der Hilst, R., 1999. The deep structure of the Australian continent from surface wave tomography. Lithos 48, 17–43.
Souther, J., Clague, J., Mathewes, R., 1987. Nazko cone: a Quaternary volcano in the eastern Anahim Belt. Can. J. Earth Sci. 24, 2477–2485.
Stacey, R.A., 1974. Plate tectonics, volcanism and the lithosphere in British Columbia. Nature 250, 133–134.
Thorkelson, D., 1996. Subduction of diverging plates and the principles of slab window formation. Tectonophysics 255, 47–63.
Thorkelson, D., Taylor, R., 1989. Cordilleran slab windows. Geology 17, 833–836.
Tilmann, J. T., 1999. The seismic structure of the upper mantle beneath Hawaii. Ph.D. thesis, Cambridge.
van der lee, S., Frederiksen, A.W., 2005. Surface-wave tomography applied to the North American upper mantle. Geophys. Monogr. 157, 67–80.
VanDecar, J., 1991. Upper-mantle structure of the Cascadia subduction zone from non-linear teleseismic travel-time inversion. Ph.D. thesis, University of Washington, Seattle.
VanDecar, J.C., Crosson, R.S., 1990. Determination of teleseismic relative phase arrival times using multi-channel cross-correlation and least-squares. B. Seismol. Soc. Am. 80, 150–169.
Wickens, A.J., 1977. The upper mantle of southern British Columbia. Can. J. Earth Sci. 14, 1100–1115.
Wickens, A.J., Buchbinder, G.G.R., 1980. S-wave residuals in Canada. B. Seismol. Soc. Am. 70, 809–822.
Wolfe, C., Th Bjarnason, I., VanDecar, J., Solomon, S., 1997. Seismic structure of the Iceland mantle plume. Nature 385, 245–247.
Yorath, C.J., Hyndman, R.D., 1983. Subsidence and thermal history of Queen Charlotte Basin. Can. J. Earth Sci 20, 135–159.
Zandt, G., Humphreys, E., 2008. Toroidal mantle flow through the western US slab window. Geology 36, 295–298.
Zielhuis, A., Nolet, G., 1994. Shear-wave velocity variations in the upper mantle beneath central Europe. Geophys. J. Int. 117, 695–715.

Please cite this article as: Mercier, J.-P., et al., Body-wave tomography of western Canada, Tectonophysics (2009), doi:10.1016/j.tecto.2009.05.030